Journal of Materials Processing Tech. 330 (2024) 118489

Contents lists available at ScienceDirect

Journal of Materials Processing Tech.

journal homepage: www.elsevier.com/locate/jmatprotec

Preparing bulk nanocrystalline Cu–Al alloys via rotary swaging

Kaixuan Zhou [a,1], Yonghao Zhao [a,b,*,1], Qingzhong Mao [a], Binpeng Zhu [a], Guosheng Sun [a], Shunqiang Li [a], Jizi Liu [a,c,*]

[a] Nano and Heterogeneous Materials Center, School of Materials Science and Engineering, Nanjing University of Science and Technology, Nanjing 210094, China
[b] School of Materials Science and Engineering, Hohai University, Changzhou 213200, China
[c] Center of Analytical Facilities, Nanjing University of Science and Technology, Nanjing 210094, China

ARTICLE INFO

Keywords:
Nanocrystalline Cu–Al alloys
Rotary swage
Strength
Deformation mechanisms

ABSTRACT

Although nanocrystalline (NC) metals and alloys have been studied for nearly 40 years, their preparation is limited to the laboratory as large-scale; low-cost commercial production remains a challenge. In this study, high-strength bulk NC Cu–Al alloys were prepared from coarse-grained Cu–Al alloy rods via rotary swaging. Rotary swaging is characterized by the low cost and infinite length of the processed samples; therefore, it can advance the industrial application of bulk NC alloys. Core–shell-structured Cu–Al alloy rods with a hard NC core (diameter of 2.2 mm) wrapped in a soft ultrafine-grained (UFG) shell with a thickness of 1.75 mm were prepared using a rotary swage. Tensile tests revealed that the hard NC Cu–Al alloy core exhibited an ultimate tensile strength of 1034 MPa, which surpassed current strength records. Microstructural characterization showed that the hard NC core was composed of NC fiber grains with widths of 45 nm and lengths of 190 nm. The edge of the rod contained numerous low-angle grain boundaries and shear bands, which provided it with a lower strength and higher elongation than those of the center. During swaging, strong (200) and (111) fiber textures perpendicular to the cross-section were produced during the early stages of deformation. In the latter deformation stages, the polar densities of the (200) and (111) textures weakened, and some complex textures were formed along with high-angle grain boundaries. The grain refinement mechanisms were dominated by multiple deformation twinning, stacking faults, and dislocation slips. Finite elemental analysis showed that triaxial compressive stress and a high strain rate were applied to grain refinement. In addition, the softer shell protects the harder core during deformation, preventing fracture. This study verified an effective preparation technique for bulk NC materials via rotary swaging because it is a simple process with low cost and broad industrial prospects.

1. Introduction

Nanostructured (NS) metals, including nanocrystalline (NC) materials with an average grain size of less than 100 nm, and ultrafine-grained (UFG) materials with an average grain size of 100–1000 nm, have been studied for 40 years [1]. The strengthening of NC metals is achieved by refining the microstructure of the material without changing their composition. Therefore, NC metals significantly reduce the dependence on alloy elements and show potential for industrial applications. Significant progress has been made in the preparation, structural characterization, and mechanical, physical, and chemical property tests of NC materials. However, a combination of low cost, easy control, high purity, and large product volume through a single preparation method has been challenging to obtain despite the development of multiple methods of preparation [2]. Therefore, the large-scale application of NC materials is still limited. To address this challenge and facilitate the industrialization of NC materials, advanced preparation technologies must be developed that simultaneously possess the above characteristics [3].

In general, the methods for preparing bulk NC materials are divided into two categories according to the order of formation: the "bottom-up" two-step method and the "top-down" one-step method [1,2]. The "bottom-up" two-step process includes an inert gas condensation and solidification method [1], as well as a mechanical alloying method (ball milling plus powder metallurgy sintering) [4], which stacks small structural units (nanoparticles or micron particles containing

* Corresponding authors at: Nano and Heterogeneous Materials Center, School of Materials Science and Engineering, Nanjing University of Science and Technology, Nanjing 210094, China.
E-mail addresses: yhzhao@njust.edu.cn (Y. Zhao), jzliu@njust.edu.cn (J. Liu).
[1] These authors contributed equally to this work

https://doi.org/10.1016/j.jmatprotec.2024.118489
Received 10 April 2024; Received in revised form 17 June 2024; Accepted 18 June 2024
Available online 20 June 2024

Table 1
Chemical compositions of the Cu–Al alloy analyzed using a direct-read spectroscopic analyzer. The elements detected in excess of 0.01 % are listed.

Elements	Al	Te	Sb	Se	S	Fe	Total others	Cu
at%	15.20	0.05	0.01	0.01	0.01	0.01	< 0.02	balance

nanograins) into macroblocks. Generally, the target metal is initially refined into micro-powders, then the microunits are densified and formed into large blocks by hot pressing. This method can be used to synthesize bulk NS materials with a grain size of less than 100 nm; however, the sample size is relatively small, and the pressing process leaves unavoidable preparation defects, such as residual pores, impurities, and microcracks in the sample (although optimized processes such as electric field assistance promote densification [5]), which cause stress concentrations and brittle fractures during service. The "top--down" one-step method directly refines coarse grain (CG) units into ultrafine grain units using severe plastic deformation (SPD) [2]. This method can be used to prepare highly dense and pure bulk NS metals. Currently, the most commonly used SPD technologies [3] include high-pressure torsion (HPT) [6], equal channel angular pressing (ECAP) [7], accumulative roll bonding (ARB) [8], multiaxial forging [9], and twist extrusion (TE) [10], as well as derivative approaches that are based on these methods.

SPD exhibits high hydrostatic pressure and high strain, with the former ensuring the smooth progress of the latter [11]. SPD methods typically exhibit significant grain refinement capabilities [12,13]; however, there are some disadvantages to using these methods, such as the small product size for ECAP and HPT [14], high precision control requirements for multi-axial forging, and possible poor interface bonding for ARB. In addition, there are some common issues such as high time costs, complex processes, and high maintenance [15]. Under constant temperature and strain rate, the stress state determines the upper limit of grain refinement, and a three-directional restricted stress state can prevent free plastic flow and accumulate more defects [11,16]. In addition, an appropriate strain must be applied to the sample. The strength of many materials is gradually saturated after a specific level of strain. Furthermore, excessive deformation results in lower returns in refinement, and even some NC alloys exhibit detwinning and grain growth phenomena in HPT [17]. Therefore, using an optimized stress state, low-cost, and large-scale continuous preparation method to appropriately deform the workpiece and obtain excellent performance products is an optimal solution for solving the industrial application limitations of NC materials.

Recently, bulk high-strength Mg–Gd–Y–Zr and AZ31 alloys [18,19], high-conductivity Cu and Cu–Cr–Zr [20,21], high-toughness Al and Al matrix composites [22,23] as well as commercially pure Ti [24] were successfully prepared by rotary swaging (RS). RS is a widely used industrial method that facilitates the high-throughput mass production of metals with enhanced mechanical properties. This near-net forming process uses a high-speed pulse hammer (multi-hammer) to process solid shaft parts or hollow tubes with variable cross-sectional areas [25,26]. As the RS process can enable large hydrostatic stresses and facilitate the accumulation of large strains, it has also been employed to improve the mechanical properties of refractory metals and alloys [26].

In this study, RS was used to address the previously mentioned challenges and produce low-cost NC materials on a large-scale. An NC alloy, with a diameter measuring on the millimeter scale and a theoretically infinite length, was prepared by deforming the coarse-grained Cu–15 at% Al alloy with low stacking fault energy (SFE). The grain refinement mechanisms and the characteristics of RS deformation were systematically studied using microstructure characterization and finite element simulation. This resulted in the recommendation of the

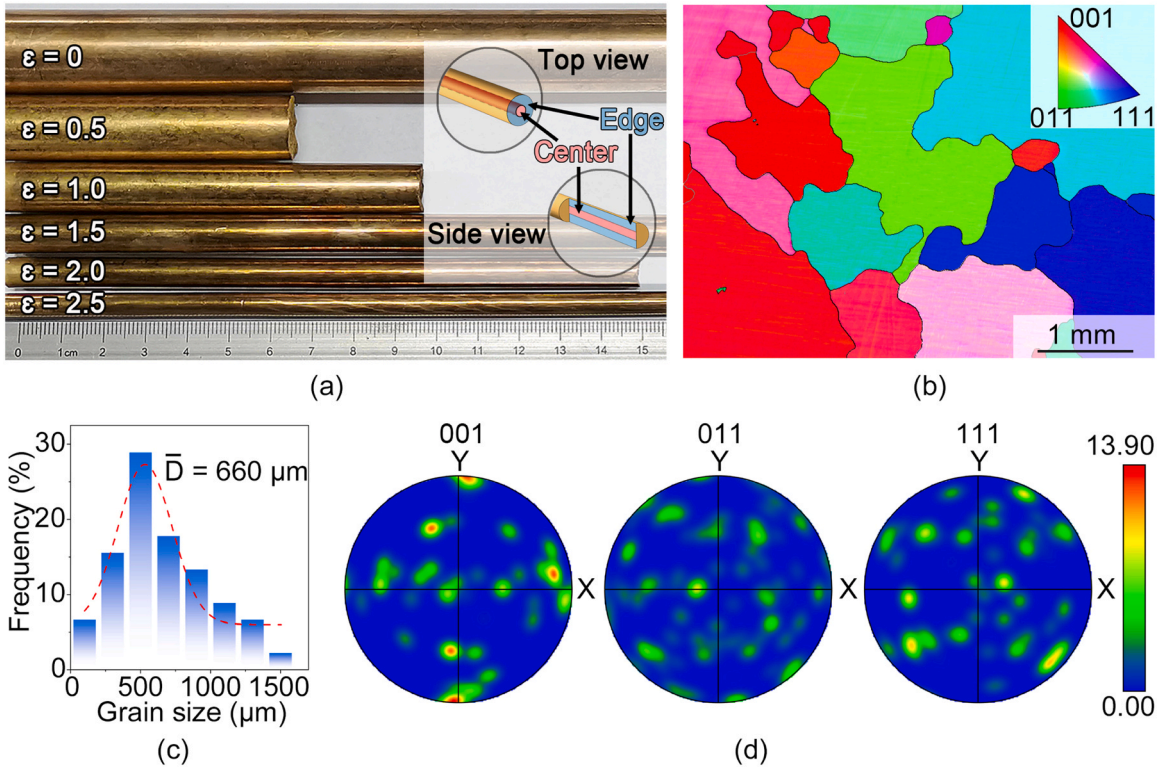

Fig. 1. (a) Image of the rotary swaging Cu–Al samples with ε=0, ε=0.5, ε=1.0, ε=1.5, ε=2.0, and ε=2.5; the inset image explains the sampling location and perspective. (b) Electron back-scattering diffraction inverse pole figure, (c) grain size distributions, and (d) pole figure of the homogenized Cu–Al alloy (ε=0).

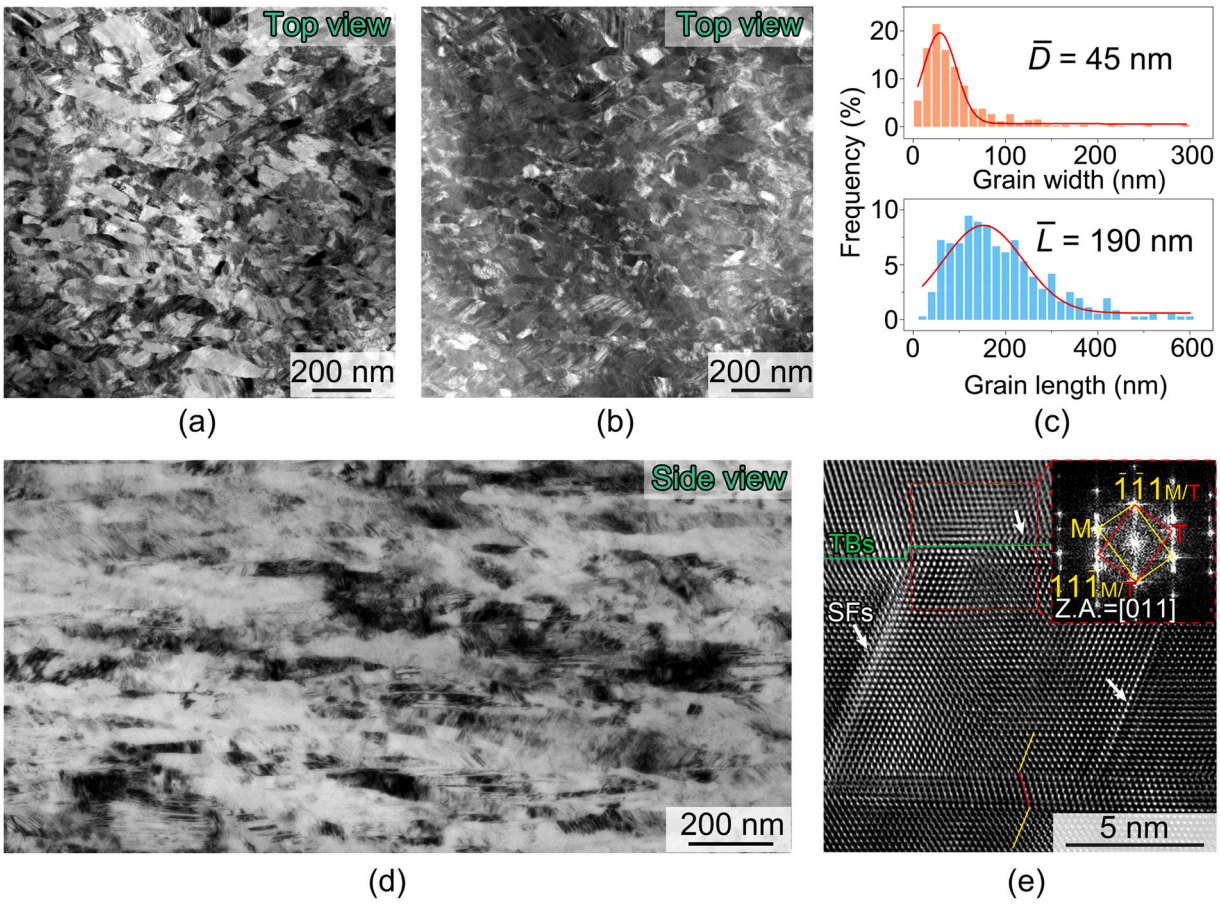

Fig. 2. Microstructure of the center of the swaged Cu–Al sample at ε=2.5. (a) STEM bright field image and (b) dark field image of the top view. (c) Grain width and length distribution. (d) Bright-field image of the side view. (e) High-resolution TEM image of (d).

following three characteristics of RS deformation: triaxial compressive stress, high strain rate, and a low deformation increase in temperature.

2. Materials and methods

2.1. Preparation of bulk NC Cu–Al

A rectangular Cu–Al alloy bar with dimensions of 50 mm ×50 mm × 300 mm was vacuum-melted and cast and then hot-forged. The chemical compositions of the Cu–Al alloys tested using a direct-read spectroscopic analyzer-Q4 TASMAN 130 (Bruker, Germany) are listed in Table 1.

The Cu–Al alloy bar was first homogenized at 1073 K for 2 h in an air-circulated furnace, then machined into Ø20 × 200 mm rods for subsequent RS processing. The homogenized CG Cu–Al alloy had an average grain size of 660 μm (Fig. 1**b,c**), a random grain orientation, and no discernable texture (Fig. 1**d**). The RS process was then performed at room temperature through multiple iterations. Subsequently, the Cu–Al rods were thinned to diameters of 15.6, 12.1, 9.4, 7.4, and 5.7 mm, which corresponded to the equivalent strains (ε) of 0.5, 1.0, 1.5, 2.0, 2.5. The formula, $\varepsilon=\ln(A_0/A)$, was used to calculate ε, where A_0 and A are the initial and final cross-sectional areas, respectively. The macroscopic images of samples with different ε values are shown in Fig. 1**a**. In this study, the planes in the two directions (top view and side view) of the RS sample were defined for representation purposes. Because the structural differences between the center and edge of the RS rod were significant, the position of the center and edge of the rod were also defined, as shown in the inset of Fig. 1**a**.

2.2. Mechanical property tests

Vickers microhardness tests were performed using an HMV-G 21DT (Shimadzu, Japan) tester with a load of 1.96 N and a dwell time of 10 s. The sample surface was mechanically polished to freshness, and 10 indentations were tested to obtain reliable results.

Uniaxial tensile tests were performed at room temperature using an Instron 5982 tester with a strain rate of $1 \times 10^{-3}\ s^{-1}$. The cross section of the tensile specimen gauge was circular, and the ratio of the section gauge diameter to the gauge length was uniform at 1:5 owing to the change in the diameter by swaging. All tensile specimens were obtained with a gauge length parallel to the swaging direction. The tensile specimens of the rod center had gauge dimensions of ϕ4.4 × 22 mm for ε=0, ϕ3.2 × 16 mm for ε=0.5, and ϕ1.2 × 6 mm for ε>0.5; in addition, the gauge dimensions of the edge and center + edge of ε=2.5 were ϕ1.2 × 6 mm and ϕ4.0 × 20 mm, respectively. The tensile strain was measured using a standard noncontact video extensometer. Three tensile specimens were tested to obtain reliable results.

2.3. Microstructural characterizations

Electron backscattering diffraction (EBSD) analysis was performed using a Zeiss Auriga focused ion beam/scanning electron microscope equipped with a fully automatic Oxford Instruments Aztec 2.0 EBSD system. The samples used for EBSD were first sandpaper-polished and mechanically polished, and then electropolished on a Buehler Electro-Met@4 with an electrolyte containing H_3PO_4 (25 %), absolute alcohol (25 %), and deionized water (50 %) at a voltage of 8 V and polishing time of 30–60 s. Software Channel5 was used to process the EBSD data.

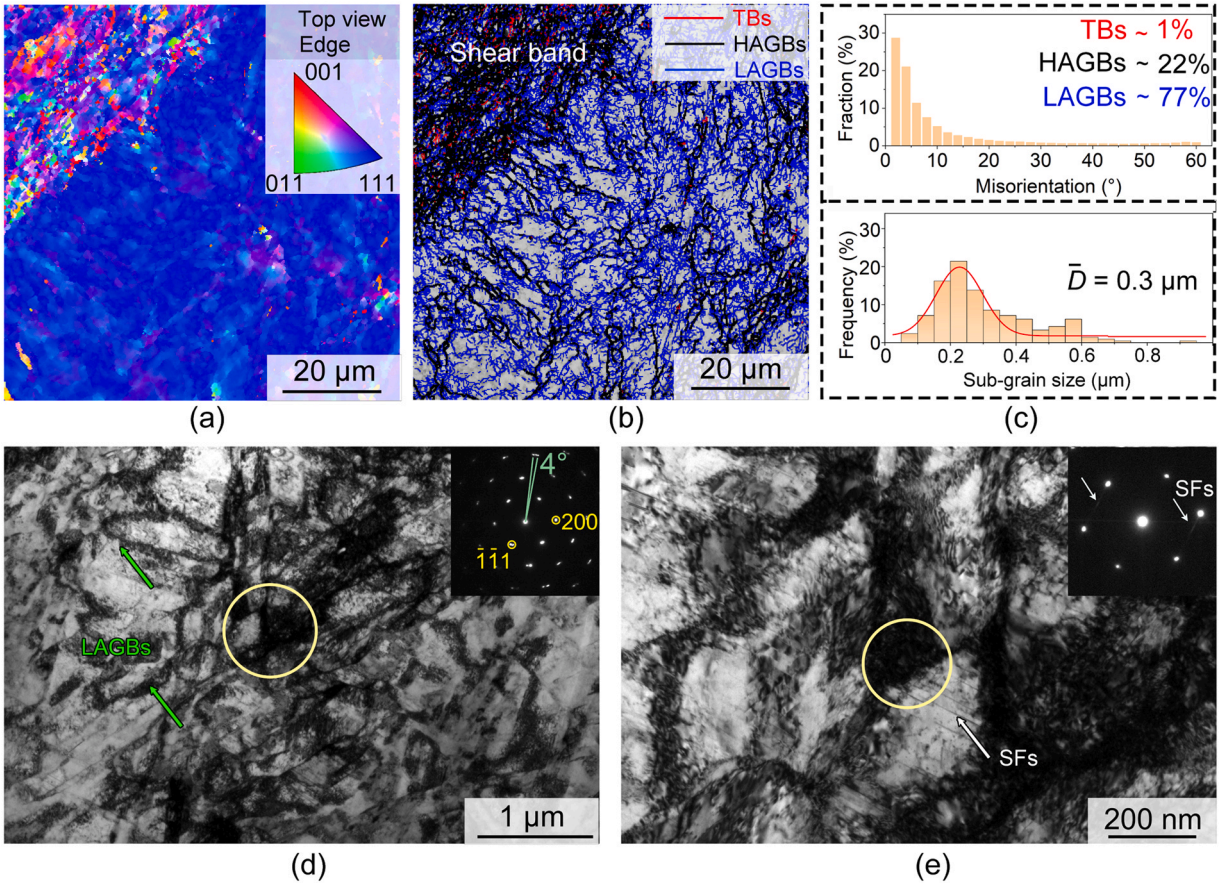

Fig. 3. Top-view electron backscatter diffraction map and TEM image of the edge of the Cu–Al sample at ε=2.5. (a) Inverse pole figure. The legend of (a) is shown in the inset image. (b) Map of the grain boundaries. (c) Grain boundary misorientation and grain size distribution. (d) TEM image. (e) High-magnification TEM image. The insets of (d) and (e) are the selected area electron diffraction patterns of the yellow circles.

Texture was tested on a SmartLab diffractometer (Rigaku) using the Schulz back-reflection method. The working voltage and current were set to 40 kV and 40 mA, respectively. Three incomplete pole maps, (200), (220), and (111), were collected in 5° increments at α and β measurement ranges of 0° to 70° and 0° to 360°, respectively.

Transmission electron microscopy (TEM), high-resolution TEM (HRTEM), and scanning transmission electron microscopy (STEM) observations of the materials were performed using a Titan G2 60–300 at a voltage of 300 kV. The tested samples were machined and sanded to obtain 50 μm thick discs, then twin-jet polished in an electrolyte containing H_3PO_4 (25 %), absolute alcohol (25 %), and deionized water (50 %) at approximately 265 K.

2.4. Finite element (FE) analysis

In this study, deform V11 commercial software was used to simulate the first-pass RS of homogenized Cu–Al (from 20 mm to 19.7 mm in diameter), and the entire component was meshed using tetrahedron elements. The initial temperature of the workpiece and dies was 20 °C; additionally, the friction coefficient between the workpiece and die was 0.12. The behavior of the material was determined by the stress–strain curve generated by the tensile test of the CG Cu–Al.

3. Results

3.1. Microstructures of the Cu–Al alloy at ε=2.5

3.1.1. Microstructure of the center of the Cu–Al alloy at ε=2.5

The top view of the STEM-bright field (BF) and -dark field (DF) images of the Cu–Al alloy at ε=2.5 showed that the hard core or the center of the swaged Cu–Al rod was composed of equiaxed relatively uniform NC grains (Fig. 2**a,b**). The average grain size was approximately 45 nm (Fig. 2**c**). The side view showed that the NC grains had an average length of 190 nm and were marginally elongated along the RS direction (Fig. 2**c,d**). In addition, a high number of twin boundaries (TBs) were observed from the top and side views; however, this was more prominent from the side view, where most TBs were parallel to the axis of the rod. HRTEM and the corresponding fast Fourier transform (FFT) images show that TB (green line) contained irregularities within its structure and stacking faults (SFs), which were caused by marginal atomic misalignments (white arrows), in some areas. Approximately seven atomic layers of fine twin lamellae (yellow and red lines) were also observed (Fig. 2**e**).

3.1.2. Microstructure of the edge of the swaged Cu–Al sample at ε=2.5

The top-view inverse pole figure (IPF) map of the edge of the Cu–Al sample at ε=2.5 shows that the preferred orientation was obtained by deformation; additionally, the randomness of the orientation of the grains refined in the shear band was higher (Fig. 3**a**). The grain boundary (GB) map shows that the sample contained many low-angle GBs (LAGBs), as shown in Fig. 3**b**. Based on the analysis of the GB misorientation distribution of adjacent grains, the quantities of TBs, HAGBs, and LAGBs were 1 %, 22 %, and 77 %, respectively, and the subgrain was composed of LAGBs with an approximate size of 0.3 μm (Fig. 3**c**).

The TEM-BF images of the ε=2.5 edge are shown in Fig. 3**d,e**. A marginal misorientation was observed within the diffraction zone (inset in Fig. 3**d**). The network structures composed of LAGBs were consistent

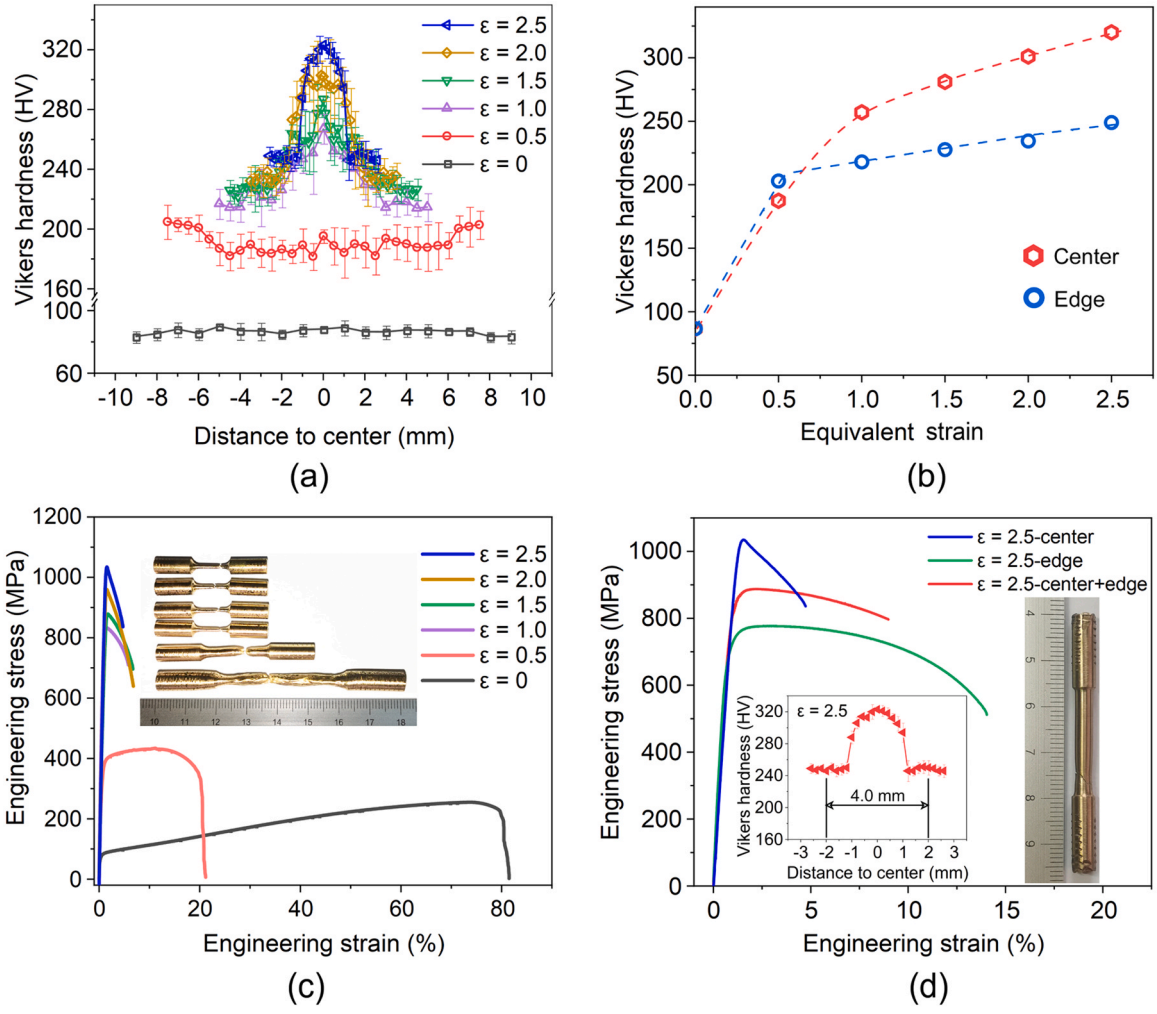

Fig. 4. Mechanical properties of the RS Cu–Al alloys. (a) Vickers microhardness measured from the center to the edge along the radial direction; the error bars represent the standard deviation of hardness. (b) Relationship between the average hardness of the center and edge versus ε. (c) Quasi-static tensile curves of the center of the RS Cu–Al alloys against ε. (d) Quasi-static tensile curves of the individual center and edge, and a combination of center and edge at ε=2.5.

with the EBSD results (green arrows in Fig. 3**e**). Moreover, there were numerous SFs inside the sub-grains, which resulted in the tailing of the diffraction spot (Fig. 3**e**).

3.2. *Mechanical properties of swaged Cu–Al alloys*

Fig. 4 shows the mechanical properties of the swaged Cu–Al alloys. Fig. 4**a** shows the microhardness distribution along the radial direction of the circular section from the top view. The initial CG sample was homogeneous as the hardness was kept constant at approximately 88 HV. When ε=0.5, the hardness distribution in the center (~180 HV) was marginally lower than that of the edge (~200 HV), indicating that the deformation strengthening at the edge was greater during the early stages of deformation. Increasing ε from 1.0 to 2.5 resulted in a significant increase in overall hardness; the hardness distribution of the center was higher than that of the edge. In addition, an increase in the ε increased the hardness of the center and edge; however, the rate of increase at the center was higher than that at the edge (Fig. 4**b**). The main factors behind these differences are discussed in *Section 4.1* .

The quasi-static tensile curves of the Cu–Al alloy at the center are shown in Fig. 4**c**. The initial CG sample exhibited a yield strength ($\sigma_{0.2}$) of 72 MPa, ultimate tensile strength (σ_{UTS}) of 255 MPa, uniform elongation (ε_u) of 74.1 %, and elongation to fracture (ε_f) of 81.5 %. When ε=0.5, $\sigma_{0.2}$ and UTS increased to 320 and 434 MPa, respectively, whereas ε_u and ε_f decreased to 11.2 % and 21.2 %, respectively. At ε values higher than 0.5, the Cu–Al alloy necked immediately after yielding. Nevertheless, its strength continued to increase as the ε value increased. The σ_{UTS} value was 1034 MPa at ε=2.5. Fig. 4**d** shows the tensile curves of the individual center and edge and a combination center and edge with ε=2.5. The σ_{UTS} of the edge is 777 MPa, and the ε_f is 14.0 %. Owing to the role of the mixture, the strength and ductility of the center and edge (887 MPa and 9 %, respectively) were between those of the individual center and edge. Only samples of ε=0 and ε=0.5 have specific uniform deformation abilities because the RS deformation

Table 2
Tensile properties of RS Cu–Al alloys. $\sigma_{0.2}$, σ_{UTS}, ε_u, and ε_f are the yield strength, ultimate tensile strength, uniform elongation, and elongation to fracture, respectively.

Samples	$\sigma_{0.2}$ (MPa)	σ_{UTS} (MPa)	ε_u (%)	ε_f (%)
ε=0, ϕ4.4×22 mm (center)	72	255	74.1	81.5
ε=0.5, ϕ3.2×16 mm (center)	320	434	11.2	21.2
ε=1.0, ϕ1.2×6 mm (center)	805	833	1.3	5.7
ε=1.5, ϕ1.2×6 mm (center)	815	879	1.7	6.7
ε=2.0, ϕ1.2×6 mm (center)	918	960	1.5	6.8
ε=2.5, ϕ1.2×6 mm (center)	1016	1034	1.5	4.8
ε=2.5, ϕ1.2×6 mm (edge)	707	777	3.1	14.0
ε=2.5, ϕ4.0×20 mm (center+edge)	800	887	2.2	9.0

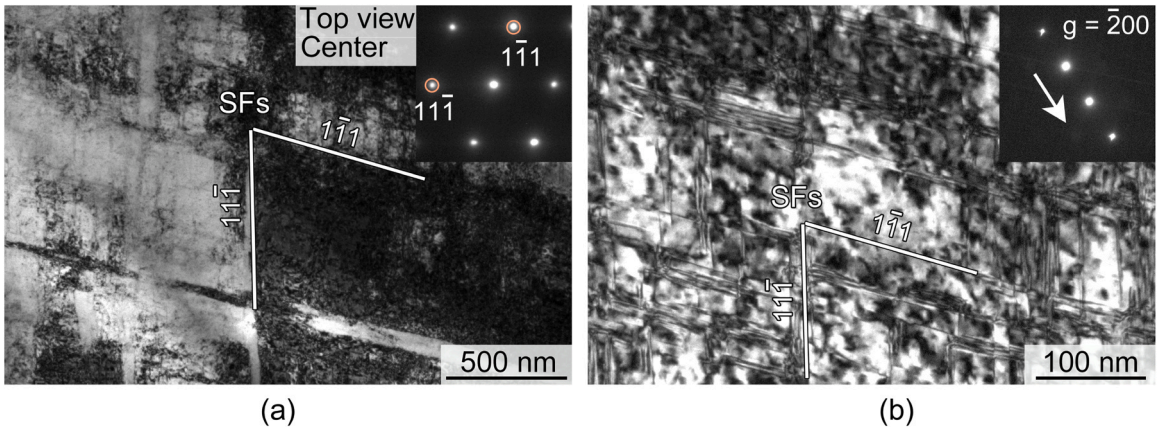

Fig. 5. Top-view TEM images of the center of the sample at ε=0.5. (a) Low magnification; the inset is the corresponding diffraction spot. (b) High magnification of the local area of (a) at g=$\bar{2}$00.

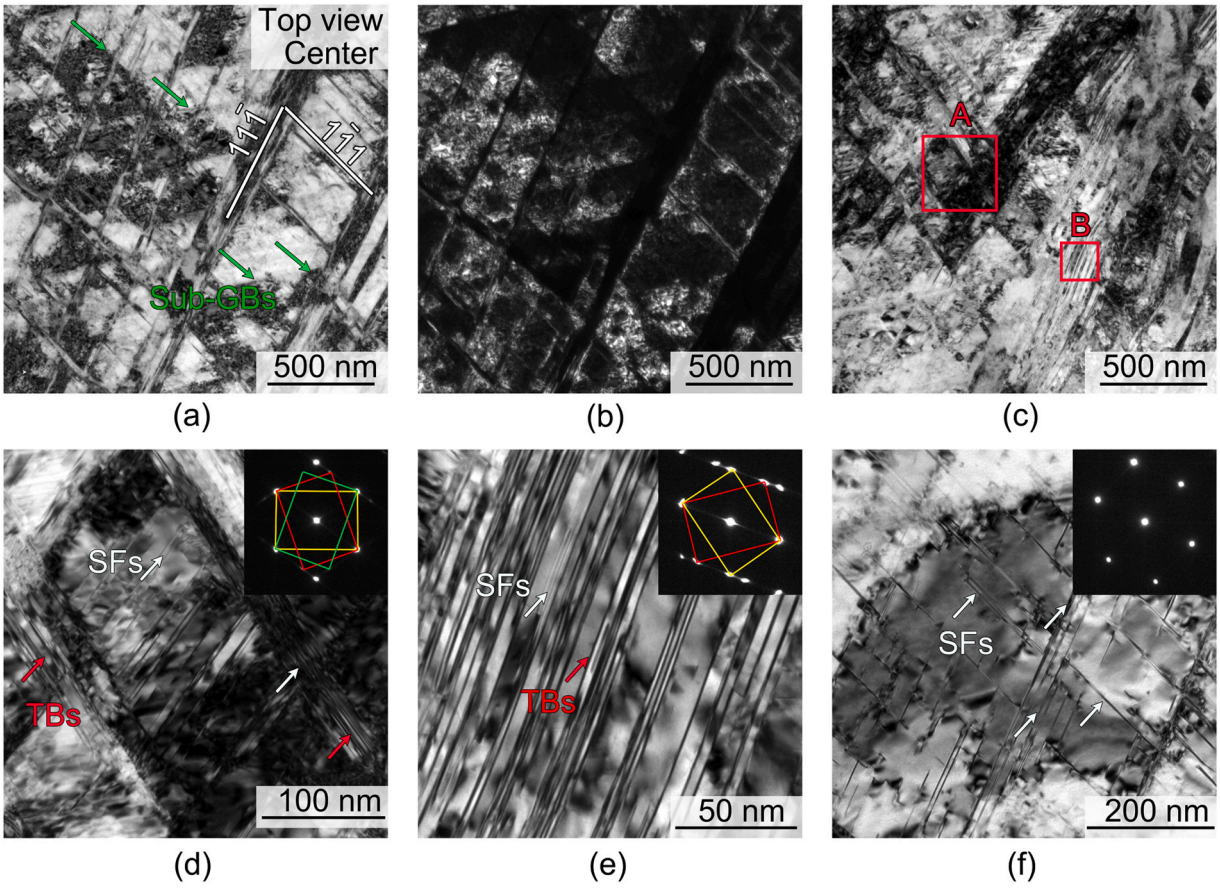

Fig. 6. Top-view TEM images of the center of the Cu–Al sample at ε=1.0. (a) and (c) Low magnification and bright-field images. (b) Dark-field image corresponding to (a). (d) and (e) Magnified images of regions A and B in (c), respectively; the insets are their corresponding selected area electron diffraction pattern. (f) Magnified TEM image showing the intersection of numerous stacking faults that further refined the coarse grains.

of samples at ε>0.5 results in internal defects that tend to saturation. Additionally, defects cannot be accumulated during the subsequent stretching process and the occurrence of strain concentration is easier, which results in macro shear bands and premature necking [27]. The tensile performance parameters are listed in Table 2.

3.3. Grain refinement process

Comprehensive TEM observations on RS Cu–Al alloys at ε=0.5, 1.0, 1.5, and 2.0 were performed to determine the refinement mechanisms of the alloy. The microstructure of the sample at ε=0.5 is shown in Fig. 5. During the initial stages of deformation, the RS Cu–Al alloy contained many SFs in the (1$\bar{1}$1) and (11$\bar{1}$) planes within the coarse grains. Multiple SFs intersected to form a network.

Numerous nanotwins were formed in two (111) planes of the Cu–Al sample when ε was increased to a value of 1.0. This resulted in CG grains that were cut by SFs and TBs and contained sub-GBs (green arrow in Fig. 6**a**). In other regions, a higher density of nanotwins and SFs were

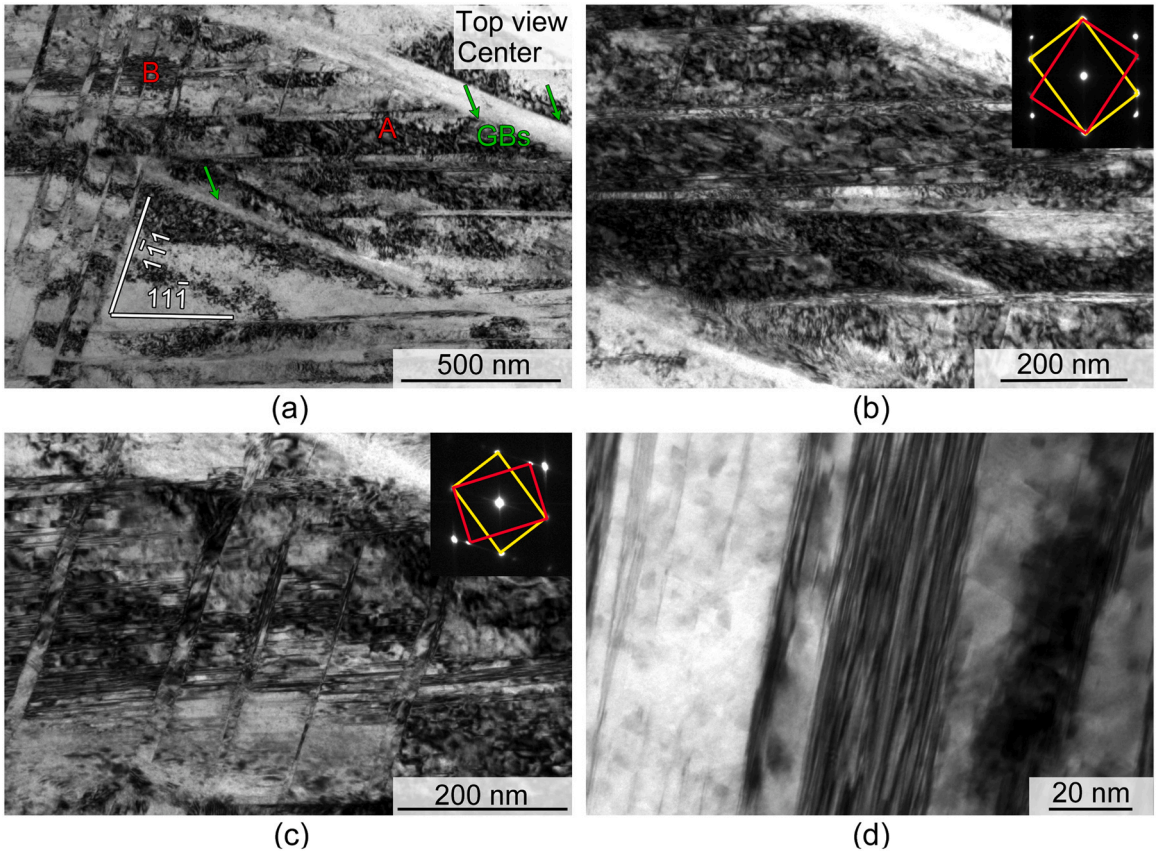

Fig. 7. Top-view TEM images of the center of the Cu–Al sample at ε=1.5. (a) Low magnification. (b) and (c) Magnified TEM images of regions A and B in (a), respectively; the insets are their corresponding diffraction. (d) Magnified TEM image showing high-density nanotwins.

observed (Fig. 6**c–e**).

Fig. 6**d**,**e** show local enlarged images of regions A and B in Fig. 6**c**, respectively. Fig. 6**d** shows numerous TBs in the two (111) planes, whereas Fig. 6**e** shows high-density and fine (less than 20 nm) unidirectional twin lamellae. Fig. 6**f** shows a magnified region where a subgrain obtained by deformation is cut by numerous SFs, which can pass through the sub-GBs. The sub-GBs have a tendency for continual refinement. Deformed TBs and SFs cut and further refined the CG grains at a deformation strain of 1.0, resulting in the formation of some subgrains.

Numerous staggered SFs and TBs were observed in the grains at an ε of 1.5, as shown in Fig. 7. In addition, new GBs were observed along a nonparallel direction to the TBs or SFs; these GBs formed elongated grains (Fig. 7**a**). Fig. 7**b**,**c** show magnified TEM images of regions A and B in Fig. 7**a**. Multiple TBs subdivided grains at ε=1.5, which was similar to that observed at ε=1.0. Additionally, some TBS were bent and transformed into HAGBs at ε=1.5 (green arrow in Fig. 7**a**) because of the accumulation of strain. Fig. 7**d** shows an SF bundle and nanotwin with a width of ~20 nm.

Some regions still contained numerous intersected SFs at ε=2.0 (Fig. 8**a–c**). However, the other regions consisted only of uniformly sized NC grains, as shown in Fig. 8**a**,**d–f**. NC grains are formed by the accumulation of numerous dislocations on TBs or SFs, resulting in their curvature and transformation into normal HAGBs [28]. At an ε value of 2.5, uniformly sized NC grains were formed (Fig. 2). The results of above grain refinement during RS explain the evolution of microhardness and yield strength, as shown in Fig. 4**a**,**c**.

As shown in Figs. 5–8, the generation and interaction of SFs, dislocations, and TBs were observed during early deformation; however, the formation of HAGBs in the coarser grains was not observed. Defects in grains gradually transformed into HAGBs after ε reached a value of 1.5. Therefore, BF-STEM was used to measure the sizes of the grains and subgrains with different orientations to reflect their microstructural characteristics (Fig. 9**a-e**). A reduction in the grain/sub-grain size was observed as the value of ε increased (Fig. 9**f**). The sizes of the grains/subgrains of the samples at ε=0, ε=0.5, ε=1.0, ε=1.5, ε=2.0, and ε=2.5 are listed in Table 3.

3.4. Texture evolution

In general, the deformation of RS results in a fiber texture perpendicular to the cross-section of the material owing to the action of radial compressive stress. Compared with the sample at ε=0, the (200) and (111) grains faced towards the axial direction; however, they were not identical (Fig. 10). The pole figure of (220) was not unique as multiple sets of spots were observed and there was a tendency towards ring formation. The orientations of <200> and <111> were concentrated at ε=1.0, with a maximum polar density of 13.62. Simultaneously, the diversity of the pole figure of <220> increased, forming a more continuous ring. This phenomenon was more pronounced at an ε value of 1.5. This texture evolution was similar to that of face-centered cubic metals and alloys deformed by RS or cold drawing [21,29].

As ε increased to 2.0, the highly oriented texture was marginally disrupted, the polar densities of (200) and (111) decreased, the rings of (220) became incomplete, and some complex textures deviated from the <200>, <220>, and <111> direction; this phenomenon was more pronounced when ε was at 2.5. As shown in Figs. 5–8, the extensive formation of HAGBs caused by deformation mainly occurred between ε values of 1.5 and 2.5, which was related to the destruction of highly oriented textures. Compared with the deformation mechanism dominated by the dislocation slip in CG materials, the generation, movement, and absence of dislocations in NC materials were significantly affected

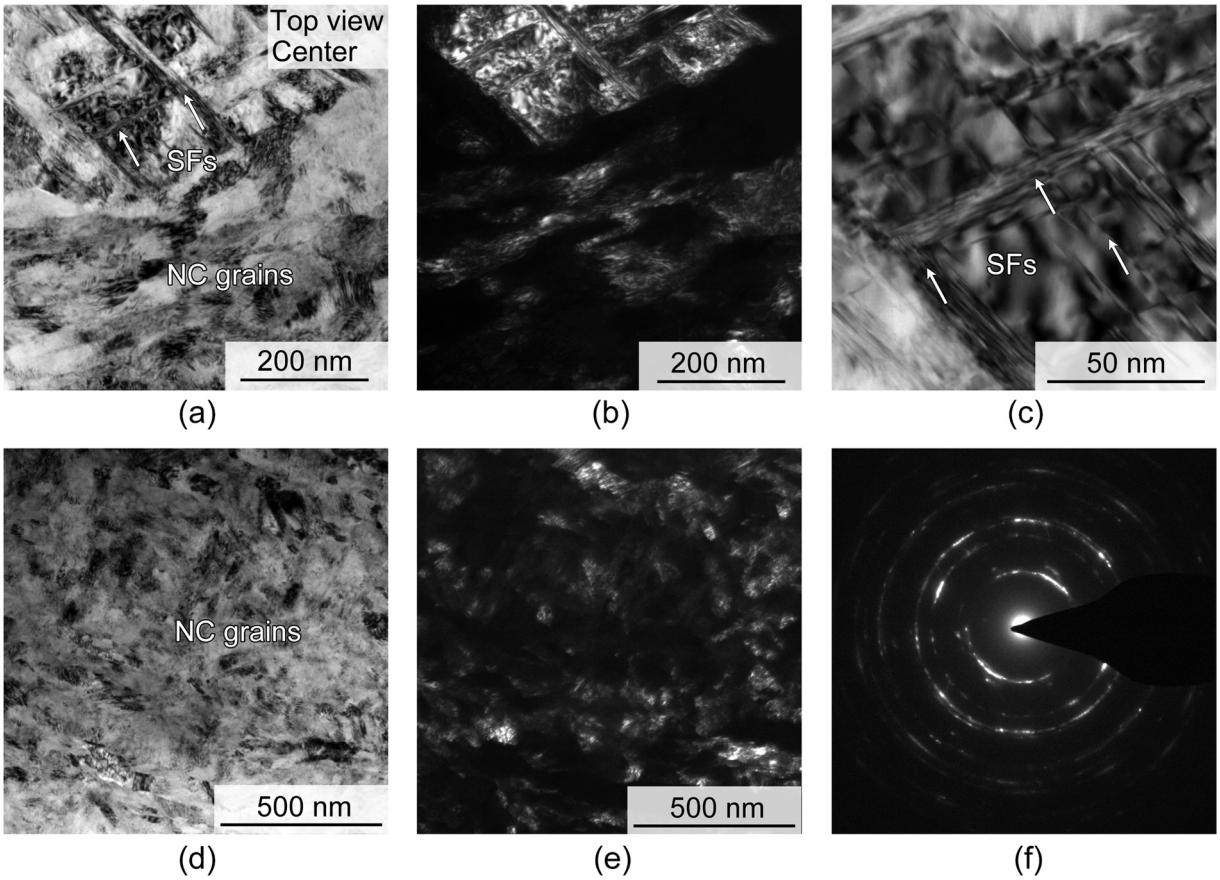

Fig. 8. Top-view TEM images of the center of the Cu–Al sample at ε=2.0. (a) and (d) Low magnification TEM images. (b) and (e) Dark-field TEM images corresponding to (a) and (d), respectively. (c) Enlarged image of the local area in (a). (f) Electron diffraction pattern of the selected area in the circular region of (d) with a diameter of 800 nm.

by GBs during the deformation process [30]. GB slip, migration, and diffusion became important deformation mechanisms [31], which influenced the secondary evolution of texture in the later stages of deformation.

3.5. Processability evaluation

RS is a near-net forming process, and product rods can be directly applied to components in various industries. Further evaluation of the processability of the NC Cu–Al rods obtained in this study (Fig. 11**a**) will help expand their scope of use. Therefore, sample ε=2.5 was further deformed by cold rolling, compression, turning, and RS, as shown in Fig. 11**b–e**. No cracking failures were observed after further treatments although the sample ε=2.5 had NC grains and extremely high strength.

4. Discussions

4.1. Preparation of nanocrystalline Cu–Al alloys

4.1.1. Working principle and parameter of the RS process

The RS deformation technique is a traditional forming process through which the diameters of rods and tubes can be reduced [32,33]. Recent studies have used this technique to perform the SPD process [34] to strengthen materials [35,36]. In the final forming process, the surface quality of the material deformed by RS was high, and the requirement for surface polishing or other treatments was limited [37,38]. Moreover, the material lost during the RS process was insignificant [25].

Based on the size of the equipment, reciprocating process of the die, and feeding process of the workpiece, the detailed parameters of the RS are listed in Table 4. The process parameters of RS can be divided into single pass and single forging. A single pass describes the process that uniformly reduces the diameter of the entire workpiece by 0.3 mm, whereas a single forging process describes the simultaneous closure of the four dies that act on the workpiece. Multiple forging processes form one pass, and multiple passes form the entire RS process. According to the estimates, a single forging required 0.0054 s, and the interval between the two forgings was 0.0405 s. The contact distance for the single forging was 0.025 mm; therefore, the diameter of the sample decreased by approximately 0.05 mm during the single forging process. The ε value for each forging varied between 0.0051 and 0.0178 based on $\varepsilon=\ln(A_0/A)$. Using the contact duration and ε, the average strain rate was estimated as 0.94–3.29 s^{-1}. Because each pass experienced the same diameter reduction (0.3 mm), the equivalent deformation for each pass was between 0.2 and 0.12 under the previously mentioned deformation.

4.1.2. Stress states of the rods during swaging

Applying large plastic strains to workpieces is challenging. Traditional forming methods are affected by internal defects and cracks in the workpiece, which can cause the material to fracture under specific strains. Research has shown that the workability of a given metal is significantly improved owing to its highly compressive stress state [39]. The workability parameter (β) is the ratio of the hydrostatic stress (σ_m) to the effective stress ($\bar{\sigma}$) [11].

$$\beta = \frac{3\sigma_m}{\bar{\sigma}} \tag{1}$$

For the three-dimensional stresses on the material, σ_m and $\bar{\sigma}$ are expressed as:

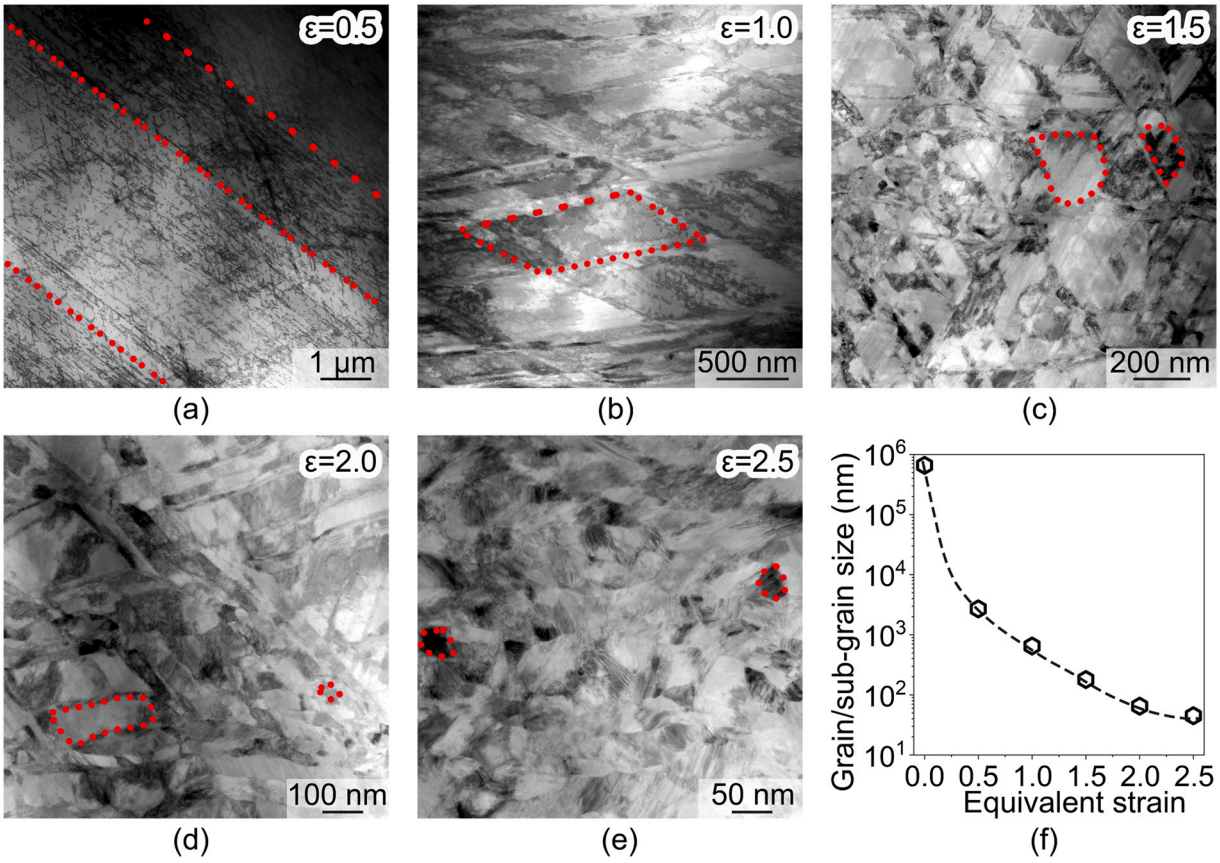

Fig. 9. Typical scanning transmission electron microscopy images of (a) ε=0.5, (b) ε=1.0, (c) ε=1.5, (d) ε=2.0, and (e) ε=2.5. (f) Average grain/sub-grain size versus ε. The red dotted line indicates the contour of some grains/sub-grains.

Table 3
Average grain/sub-grain size of samples at ε=0, ε=0.5, ε=1.0, ε=1.5, ε=2.0, and ε=2.5.

Samples	ε=0	ε=0.5	ε=1.0	ε=1.5	ε=2.0	ε=2.5
Grain/sub-grain size	660 μm	2.7 μm	650 nm	180 nm	65 nm	45 nm

$$\sigma_m = \frac{\sigma_1 + \sigma_2 + \sigma_3}{3} \tag{2}$$

$$\overline{\sigma} = \frac{1}{\sqrt{2}}[(\sigma_1 - \sigma_2)^2 + (\sigma_2 - \sigma_3)^2 + (\sigma_3 - \sigma_1)^2]^{1/2} \tag{3}$$

The β value in the basic forming tests of tension, torsion, and compression are 1, 0, and −1, respectively. The more negative the value of β, the more favorable the stress state is for plastic deformation. Therefore, compared with traditional molding methods, SPD often prevents the free flow of materials during deformation by designing special molds while applying high hydrostatic pressure and enabling them to withstand higher strain, resulting in the successful preparation of UFG and NC materials [11].

An et al. [40] showed that the workability of the alloy was more stringent as the SFE decreased. During the ECAP process, high SFE materials (~ 24–200 J/m^2) can be refined through dislocation subdivision, medium SFE materials (~ 8–24 J/m^2) can be refined through twinning fragmentation, and macroscopic fractures of alloys below 8 J/m^2, such as Cu-16Al (similar composition to the alloy in this study), only occurred in three passes (ε ~ 3); the latter was caused by the saturation of the shear bands. However, the ε of materials with the same composition can surpass 100 under HPT deformation [41]. The stress state is the main reason for the different behaviors of the same material in the processes of ECAP and HPT; however, the two SPD methods mainly rely on shear deformation, and the hydrostatic pressure applied by HPT was higher.

RS deformation also exhibited an optimized stress state. Based on the RS parameters, an FE simulation of the first-pass deformation was conducted, as shown in Fig. 12. There was a significant difference in stress distribution between the center and the edge during the deformation process. The center was subjected to triaxial compressive stress, whereas the edge was subjected to tensile and compressive stresses in different directions and positions, which were attributed to the uneven direct contact between the rod and dies (Fig. 12**a,b**). These findings were similar to the FE simulation results of RS on the deformation of rod-shaped workpieces from previous studies [42]. In addition, direct contact with the dies resulted in a marginally higher Mises strain and effective strain rate at the edge than those at the center (Fig. 12**c,d**). This resulted in the variation of hardness distribution with ε during the RS process. Therefore, a marginally higher strain and strain rate in a homogenized alloy with low dislocation density resulted in a higher deformation strengthening of the edge, which gradually saturated as the crystal defect density increased (up to ε=0.5). At this time, the free plastic flow of the material during deformation is avoided as much as possible in the three-dimensional constrained in center. Additionally, the action of axisymmetric force from the dies and the accumulation of multiple passes of strain increased the forging permeability, providing a hardness distribution that was higher in the center than the edge (ε>0.5).

The die directly acted on the surface. Because of the higher volume ratio of GBs, the fracture toughness of NC grains is often low (as shown in Fig. 4; after necking, the elongation of the center is lower than that of UFG at the edge), making them prone to fracture when subjected to non-

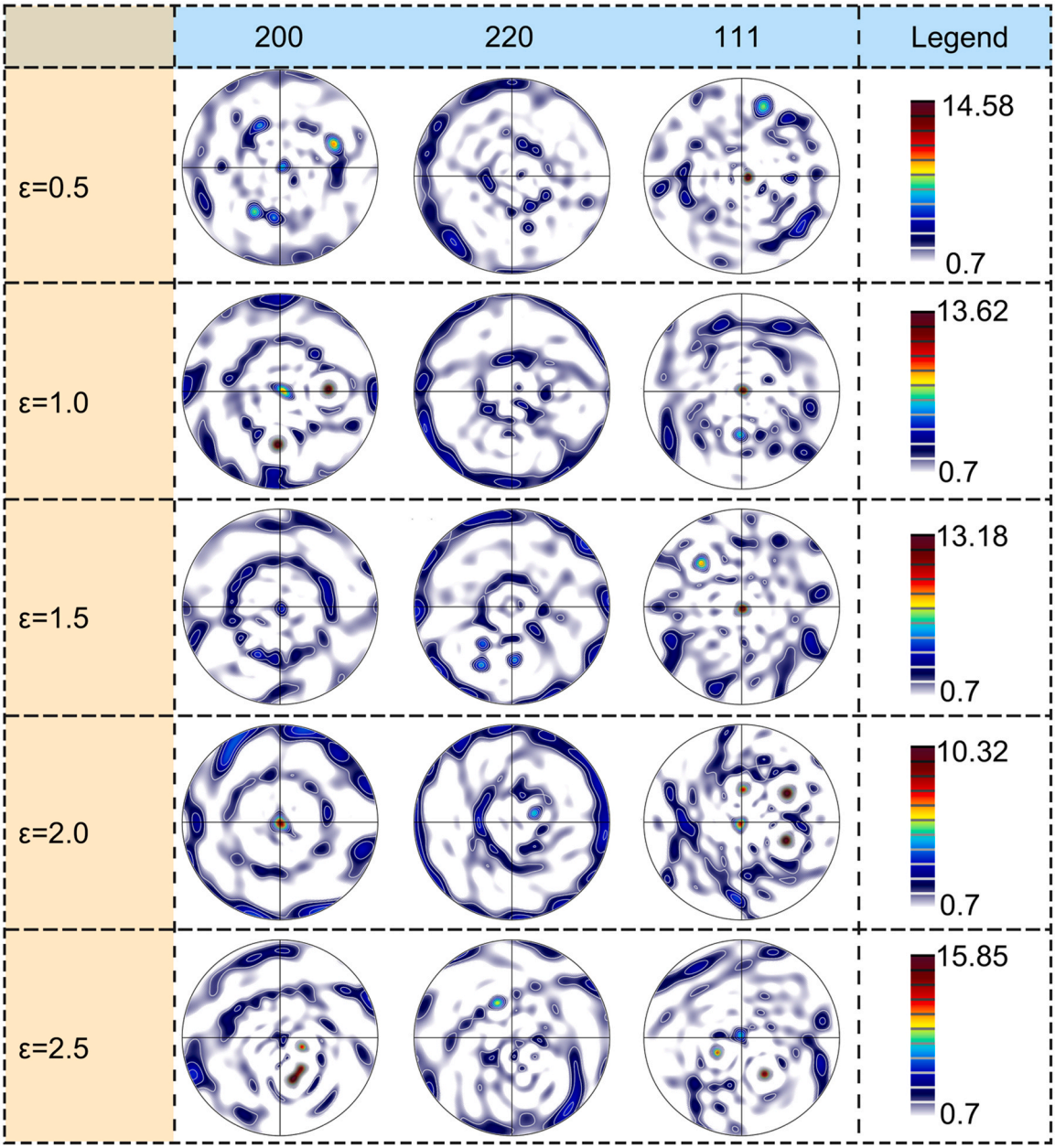

Fig. 10. Pole figure of the top view of samples at ε values ranging from 0.5 to 2.5 in the (200), (220), and (111) planes based on X-ray diffraction analysis.

three-dimensional confinement deformation. By wrapping in a shell with better plasticity, direct conduction between the dies and the NC grains was avoided, thus facilitating further deformation.

4.1.3. Balanced strain and increase in temperature

In addition to the stress state, the minimum saturated grain size in SPD is affected by the temperature, strain rate, strain, composition of the metal, and pre-strain [11]; additionally, sufficient strain is required to obtain the minimum grain size. The temperature increase caused by external deformation during cold deformation must be addressed, particularly in NC materials with low thermal stability. Considering the uniaxial case as an example, the heat generated during plastic deformation (dQ) can be calculated using the following equation [43]:

$$dQ = \beta_T \bullet \sigma \bullet V \bullet d\varepsilon_p \tag{4}$$

where β_T is the Taylore–Quinney coefficient, which describes the fraction of plastic work converted into heat. σ is stress, V is volume, and $d\varepsilon_p$ is the increment of plastic strain. Therefore, more heat is generated when the $d\varepsilon_p$ of one plastic deformation increases. Generally, the process is considered adiabatic when the strain rate exceeds 1 s^{-1}; therefore, heat is not transferred to the surroundings, which likely increases the temperature.

The average strain rate ($\dot{\varepsilon}$), ε, contact duration (t) has the following relationship during one plastic deformation [44]:

$$\dot{\varepsilon} = \frac{\varepsilon}{t} \tag{5}$$

From Equ. (4) and Equ. (5), it can be concluded that in order to achieve high strain, high strain rate, and low plastic deformation temperature rise for grain refinement, only a small quantity and rapid deformation in one pass was required, and sufficient time between passes to cool the material. According to Table 4, the ε of a single pass was between 0.03 and 0.11, and the strain rate can vary between 0.94 and 3.29 s^{-1}. This is an important factor in the preparation of NC materials.

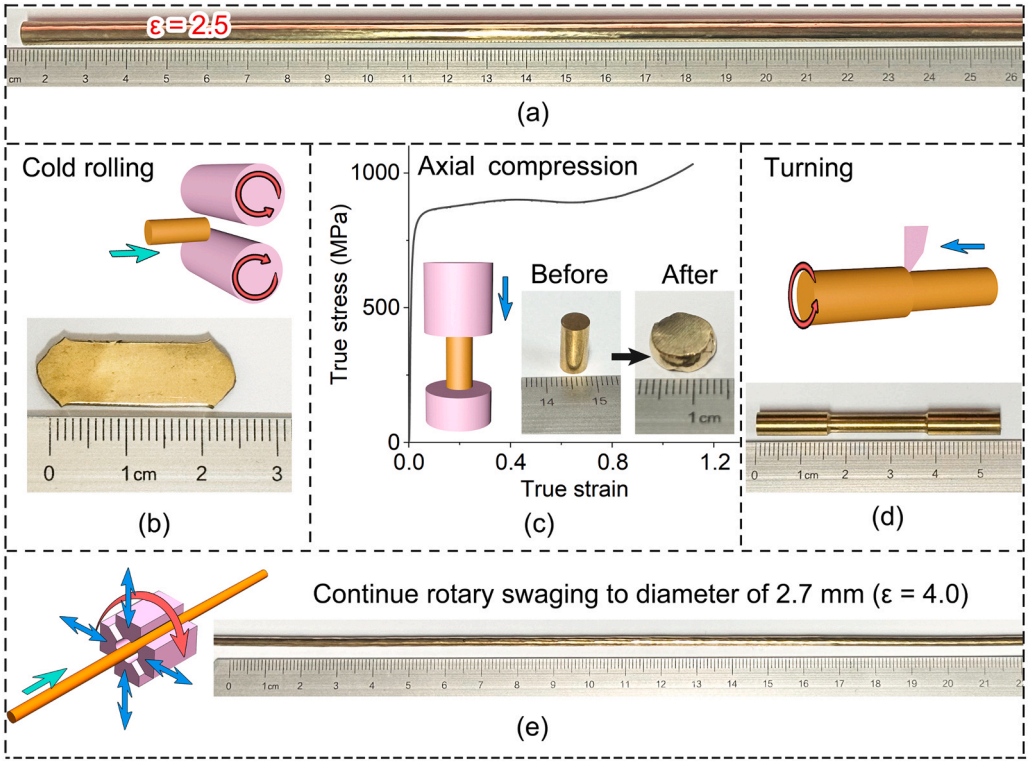

Fig. 11. Processability evaluation of a sample at ε=2.5. Image of (a) sample at ε=2.5 and its subsequent (b) cold rolling, (c) axial compression, (d) turning, and (e) rotary swaging. The thickness reduction for each rolling pass was 0.3 mm until the thickness reached 1 mm. The strain rate for axial compression was 1×10^{-3}, and the specimen was compressed from a height of 11.56–3.73 mm. The above treatments did not inflict material fracture.

Table 4
Parameters for rotary swaging deformation used in this study.

Index	Value
Feed rate	17 mm/s
Rotation speed	654°/s
Reduction in diameter per pass	0.3 mm
Equivalent strain for one pass	0.03–0.11
Single forging contact duration	0.0054 s
Two forging interval duration	0.0405 s
Single forging diameter reduction	0.05 mm
Single forging equivalent strain	0.0051–0.0178
Single forging strain rate	0.94–3.29 s^{-1}

4.2. Grain refinement mechanisms

A schematic of the grain refinement process (Fig. 13) was generated based on the TEM results (Fig. 2 and Figs. 5–8). The processes with increasing ε from 0 to 2.5 correspond to Fig. 13**a–f**, respectively. The refinement of the NC grains in the rod center can be divided into the following steps: I. Generation of numerous SFs. II. Formation of twins. III. Transformation of TBs into GBs and formation of secondary TBs. IV. Formation of numerous NC Grains. V. Continual refinement to form NC grains that are uniform and/or relatively uniform in size. The refinement of NC grains depended on the interaction between SFs, TBs, and dislocations; however, the impact of twinning was dominant.

The deformation strengthening rates of the center and edge of the rod were higher at ε values in the early stages (ε<0.5) than those in the later stages (0.5<ε<2.5) (Fig. 4), it can be observed that both the center and edge of the rod have better deformation strengthening rates with ε in the early stage than in the later stage, correspondingly, the refinement efficiency of grain/sub-grain size is also more pronounced in the early stages (Fig. 9). This is due to that in the early stages of deformation, the number of dislocations and SFs inside the material rapidly increases, and

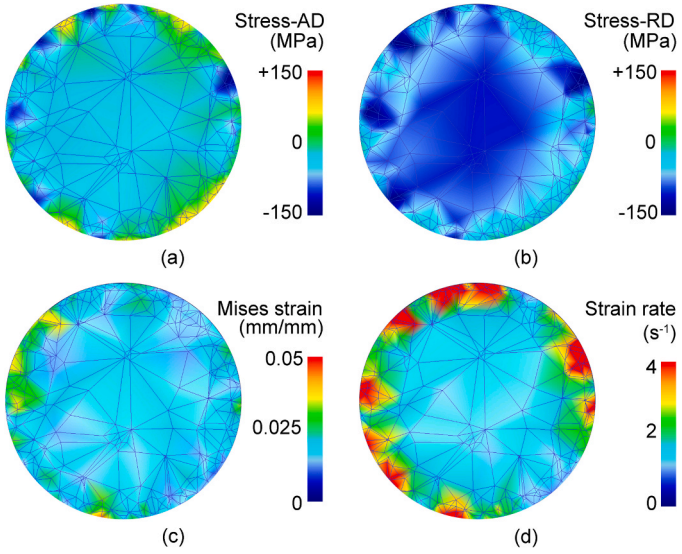

Fig. 12. Finite element analysis of the rotary swaging process in the first pass of this study. Distributions of (a) axial direction stress (AD), (b) radial direction stress (RD), (c) Mises strain, and (d) effective strain rate. In (a) and (b), positive and negative values represent tensile stress and compressive stress, respectively.

the interaction between them leads to an increase in material hardness and strength. As ε increases, due to the limited ability of defect accumulation inside grains, the rate of dislocation annihilation increases, in addition, the later stage of deformation involves the transformation of TBs to HAGBs, both of the TBs and HAGBs have a pinning effect on dislocations to contribute strength. Therefore, the deformation

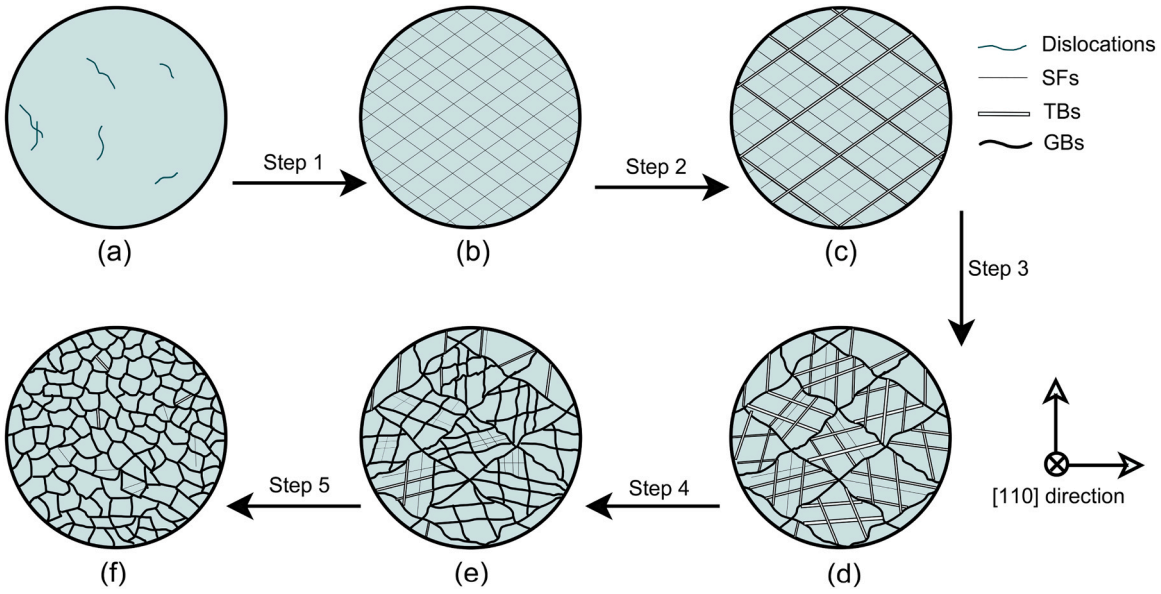

Fig. 13. Schematic of the grain refinement mechanism of the rotary swaging Cu–Al alloy.

strengthening is more obvious in the early deformation stage.

The slope of the hardness versus ε of the center was more positive than that of the edge when ε varied between 1.0 and 2.5 (Fig. 4**b**) because of the different stress states between the center and edge. During the early stages of the deformation of CG alloys with middle or low SFE values, the slip of full dislocations was often dominant; additionally, an increase in stress concentrations was observed inside the material as the dislocation density increased [45]. Twinning may occur when the dominant slip system changes and the critical shear stress for twinning is attained [46]. Therefore, the ease of twinning activation in this instance was greater because the critical shear stress was lower than the full dislocation slip. This introduced the critical dislocation density (ρ_n). When the dislocation density value caused by deformation in the material is higher than ρ_n, twinning will be promoted as follows [47]:

$$\rho_n = \frac{\gamma^2}{G^2 b_1^2} \bullet \frac{1}{(n\alpha b - b_1)^2} \tag{6}$$

where γ is the SFE of the alloy, G is the shear modulus, n is the stress concentration factor, and b_1 and b are the Burgers vector of Shockley partial dislocations and full dislocations, respectively. The ability of dislocations to accumulate varies under different stress states. In this study, the direction of stress given by the dies was more random at the edge, and the microstructure exhibited coordinated deformation through dislocations and SFs rather than twinning; however, the center of the sample achieved the condition for twinning and produced numerous TBs. TBs facilitated significantly more grain refinements than those of dislocations, which resulted in different deformation and grain refinement mechanisms between the center and the edge. Additionally, this resulted in more noticeable differences between the hardness and microstructure at the interface with increasing ε.

5. Conclusion

In this study, high-strength bulk nanocrystalline Cu–Al alloys were prepared from coarse-grained Cu–Al alloy rods using rotary swaging. The final deformation strain of ε was 2.5. Rotary swaging is characterized by the low cost and infinite length of the processed samples and can be implemented to advance the industrial application of bulk nanocrystalline alloys. The findings of this study are summarized as follows.

1. After multiple passes of swaging deformation, nanocrystalline grains with a width of 45 nm and a length of 190 nm were obtained at the center of the rod. The ultimate tensile strength was 1034 MPa, and numerous low-angle grain boundaries and shear bands were constructed at the edge of the rod with lower strength and higher elongation than that of the center.
2. Finite elemental analysis showed that the center exhibited triaxial compressive stress and lower plastic flow. The edge was subjected to stress in a more random direction and exhibited a high plastic flow.
3. The grain refinement mechanism of the NC grains included the following steps: I. Generation of numerous stacking faults. II. Formation of twins. III. Transformation of twin boundaries and stacking faults into GBs and formation of secondary twin boundaries. IV. Formation of numerous nanocrystalline grains. V. Continual refinement to form uniform and randomly oriented nanocrystalline grains.
4. Early deformation mainly produced strong (200) and (111) fiber textures perpendicular to the cross-section. Under larger deformations, accompanied by the formation of high-angle grain boundaries, the polar densities of the (200) and (111) textures weakened, and some complex textures were formed.
5. Three characteristics of the RS deformation are recommended: triaxial compressive stress, high strain rate, and a low rate of increase of the deformation temperature, which can inspire the development of infinite-length NC materials.

CRediT authorship contribution statement

Jizi Liu: Writing – review & editing, Methodology, Investigation, Funding acquisition, Formal analysis, Conceptualization. **Shunqiang Li:** Methodology. **Kaixuan Zhou:** Writing – review & editing, Writing – original draft, Visualization, Methodology, Investigation, Formal analysis. **Qingzhong Mao:** Investigation, Funding acquisition. **Yonghao Zhao:** Writing – review & editing, Supervision, Project administration, Investigation, Funding acquisition, Formal analysis. **Guosheng Sun:** Methodology, Investigation. **Binpeng Zhu:** Methodology.

Declaration of Competing Interest

The authors declare that they have no known competing financial interests or personal relationships that could have appeared to influence the work reported in this paper.

Acknowledgements

The authors would like to acknowledge financial supports from National Key Research and Development Program of China (Grant No. 2021YFA1200203), National Natural Science Foundation of China (Grant No. 51971112, 51225102, and 52171119), Jiangsu Province Leading Edge Technology Basic Research Major Project (BK20222014), Fundamental Research Funds for the Central Universities (No. 2023201001), Jiangsu Funding Program for Excellent Postdoctoral Talent (Grant No. 2023ZB091), and China Postdoctoral Science Foundation (Grant No. 2023M741699). The authors also want to acknowledge the support of the Jiangsu Key Laboratory of Advanced Micro-Nano Materials and Technology. SEM, TEM and EBSD experiments are performed at the Center of Analytical Facilities of Nanjing University of Science and Technology. Thanks to Miss Ming Yang for the help on visualization. Thanks to eceshi (www.eceshi.com) for the XRD texture test.

References

[1] Gleiter, H., 1989. Nanocrystalline materials. Prog. Mater. Sci. 33, 223–315.
[2] Valiev, R.Z., Islamgaliev, R.K., Alexandrov, I.V., 2000. Bulk nanostructured materials from severe plastic deformation. Prog. Mater. Sci. 45, 103–189.
[3] Estrin, Y., Vinogradov, A., 2013. Extreme grain refinement by severe plastic deformation: a wealth of challenging science. Acta Mater. 61, 782–817.
[4] Lin, Y.J., Wen, H.M., Li, Y., Wen, B., Liu, W., Lavernia, E.J., 2014. Stress-induced grain growth in an ultra-fine grained Al alloy. Metall. Mater. Trans. A 45, 2673–2688.
[5] Li, X., Wang, J., Zhao, Y., Ke, H., Sun, Z., Yang, C., Wang, W., 2022. Uncovering electromigration effect on densification during electrical field assisted sintering. J. Mater. Process. Technol. 307, 117630.
[6] Zhilyaev, A.P., Langdon, T.G., 2008. Using high-pressure torsion for metal processing: fundamentals and applications. Prog. Mater. Sci. 53, 893–979.
[7] Zhao, Y.H., Liao, X.Z., Jin, Z., Valiev, R.Z., Zhu, Y.T., 2004. Microstructures and mechanical properties of ultrafine grained 7075 Al alloy processed by ECAP and their evolutions during annealing. Acta Mater. 52, 4589–4599.
[8] Saito, Y., Utsunomiya, H., Tsuji, N., Sakai, T., 1999. Novel ultra-high straining process for bulk materials—development of the accumulative roll-bonding (ARB) process. Acta Mater. 47, 579–583.
[9] Han, B., Xu, Z., 2008. Grain refinement under multi-axial forging in Fe–32%Ni alloy. J. Alloy. Compd. 457, 279–285.
[10] Beygelzimer, Y., Kulagin, R., Estrin, Y., Toth, L.S., Kim, H.S., Latypov, M.I., 2017. Twist extrusion as a potent tool for obtaining advanced engineering materials: a review. Adv. Eng. Mater. 19, 1600873.
[11] Faraji, G., Kim, H.S., Kashi, H.T., 2018. Severe Plastic Deformation: Methods, Processing and Properties. Elsevier.
[12] Zhang, Z., Yuan, L., Zheng, M., Wei, Q., Shan, D., Guo, B., 2023. Achievement of high strength and good ductility in the large-size AZ80 Mg alloy using a designed multi-directional forging process and aging treatment. J. Mater. Process. Technol. 311, 117828.
[13] Chen, Z., Zheng, J., Zhang, Z., Xue, Y., 2023. Effects of die motion parameters on the microstructures and mechanical properties of rotary backward extruded AZ80 alloys. J. Mater. Process. Technol. 319, 118081.
[14] Mohd Yusuf, S., Lim, D., Chen, Y., Yang, S., Gao, N., 2021. Tribological behaviour of 316L stainless steel additively manufactured by laser powder bed fusion and processed via high-pressure torsion. J. Mater. Process. Technol. 290, 116985.
[15] Miyajima, Y., Yamada, T., Fujii, T., 2022. Plastic instability criterion based on new necking parameters for Cu–Al, Cu–A5052, and Cu–A5083 roll-bonded laminated metal composites fabricated without post-annealing. J. Mater. Process. Technol. 306, 117634.
[16] Tian, S., Liu, X., Wang, W., Sun, Y., 2023. Deformation behavior and microstructure formation mechanism at the interface of Mg/Al composite plate during vibration assisted rolling process. J. Mater. Process. Technol. 322, 118184.
[17] Ni, S., Wang, Y.B., Liao, X.Z., Li, H.Q., Figueiredo, R.B., Ringer, S.P., Langdon, T.G., Zhu, Y.T., 2011. Effect of grain size on the competition between twinning and detwinning in nanocrystalline metals. Phys. Rev. B 84, 235401.
[18] Wan, Y.C., Tang, B., Gao, Y.H., Tang, L.L., Sha, G., Zhang, B., Liang, N.N., Liu, C. M., Jiang, S.N., Chen, Z.Y., Guo, X.Y., Zhao, Y.H., 2020. Bulk nanocrystalline high-strength magnesium alloys prepared via rotary swaging. Acta Mater. 200, 274–286.
[19] Chen, X., Liu, C.M., Wan, Y.C., Jiang, S.N., Chen, Z.Y., Zhao, Y.H., 2021. Grain refinement mechanisms in gradient nanostructured AZ31B Mg alloy prepared via rotary swaging. Metall. Mater. Trans. A 52, 4053–4065.
[20] Zhou, K., Zhao, Y., Dong, H., Mao, Q., Jin, S., Feng, M., Zhang, R., Li, S., Liu, J., 2024. Fractal structure and nano-precipitates break comprehensive performance limits of CuCrZr alloys. Nano Today 56, 102234.
[21] Mao, Q.Z., Zhang, Y.S., Liu, J.Z., Zhao, Y.H., 2021. Breaking material property trade-offs via macrodesign of microstructure. Nano Lett. 21, 3191–3197.
[22] Yang, Y., Nie, J.F., Mao, Q.Z., Zhao, Y.H., 2019. Improving the combination of electrical conductivity and tensile strength of Al 1070 by rotary swaging deformation. Results Phys. 13, 102236.
[23] Nie, J.F., Lu, F.H., Huang, Z.W., Ma, X., Zhou, H., Chen, C., Chen, X., Yang, H.B., Cao, Y., Liu, X.F., Zhao, Y.H., Zhu, Y.T., 2020. Improving the high-temperature ductility of Al composites by tailoring the nanoparticle network. Materialia 9, 100523.
[24] Meng, A., Chen, X., Nie, J.F., Gu, L., Mao, Q.Z., Zhao, Y.H., 2021. Microstructure evolution and mechanical properties of commercial pure titanium subjected to rotary swaging. J. Alloy. Compd. 859, 158222.
[25] Mao, Q.Z., Chen, X., Li, J.S., Zhao, Y.H., 2021. Nano-gradient materials prepared by rotary swaging. Nanomaterials 11, 2223.
[26] Mao, Q.Z., Liu, Y.F., Zhao, Y.H., 2022. A review on mechanical properties and microstructure of ultrafine grained metals and alloys processed by rotary swaging. J. Alloy. Compd. 896, 163122.
[27] Zhou, K., Zhao, Y., Mao, Q., Zhang, R., Li, S., Sun, G., Dong, H., Gu, L., Liu, J., 2024. Simultaneously enhancing strength and ductility of coarse grain Cu–Al alloy via a macro dual-cable structure. Compos. Part B-Eng. 276, 111371.
[28] Wang, Y.B., Liao, X.Z., Zhao, Y.H., Lavernia, E.J., Ringer, S.P., Horita, Z., Langdon, T.G., Zhu, Y.T., 2010. The role of stacking faults and twin boundaries in grain refinement of a Cu–Zn alloy processed by high-pressure torsion. Mater. Sci. Eng. A 527, 4959–4966.
[29] Chen, J., Ma, X., Yan, W., Xia, F., Fan, X., 2014. Effect of transverse grain boundary on microstructure, texture and mechanical properties of drawn copper wires. J. Mater. Sci. Technol. 30, 184–191.
[30] Valiev, R.Z., Zhilyaev, A.P., Langdon, T.G., 2013. Bulk Nanostructured Materials: Fundamentals and Applications. John Wiley & Sons.
[31] Meyers, M.A., Mishra, A., Benson, D.J., 2006. Mechanical properties of nanocrystalline materials. Prog. Mater. Sci. 51, 427–556.
[32] Ortmann-Ishkina, S., Charni, D., Herrmann, M., Liu, Y., Epp, J., Schenck, C., Kuhfuss, B., 2021. Development of residual stresses by infeed rotary swaging of steel tubes. Arch. Appl. Mech. 91, 3637–3647.
[33] Yuan, L.H., Wang, W.R., Yang, M.Y., Li, Y., Zhang, H., Zhang, H., Zhang, W.F., 2021. Microstructure and texture of thin-walled Ti-6Al-4V alloy seamless tubing manufactured by cold-rotary swaging. Jom 73, 1786–1794.
[34] Trojanová, Z., Drozd, Z., Halmešová, K., Džugan, J., Škraban, T., Minárik, P., Németh, G., Lukáč, P., 2020. Strain hardening in an AZ31 alloy submitted to rotary swaging. Materials 14, 157.
[35] Mao, Q.Z., Wang, L., Nie, J.F., Zhao, Y.H., 2022. Enhancing strength and electrical conductivity of Cu–Cr composite wire by two-stage rotary swaging and aging treatments. Compos. Part B-Eng. 231, 109567.
[36] Lu, F.H., Nie, J.F., Ma, X., Li, Y.S., Jiang, Z.W., Zhang, Y., Zhao, Y.H., Liu, X.F., 2020. Simultaneously improving the tensile strength and ductility of the AlNp/Al composites by the particle's hierarchical structure with bimodal distribution and nano-network. Mater. Sci. Eng. A 770, 138519.
[37] Yang, Y., Chen, X., Nie, J.F., Wei, K., Mao, Q.Z., Lu, F.H., Zhao, Y.H., 2021. Achieving ultra-strong Magnesium–lithium alloys by low-strain rotary swaging. Mater. Res. Lett. 9, 255–262.
[38] Mao, Q.Z., Zhang, Y.S., Guo, Y.Z., Zhao, Y.H., 2021. Enhanced electrical conductivity and mechanical properties in thermally stable fine-grained copper wire. Commun. Mater. 2 (1), 9.
[39] Dieter, G.E., Kuhn, H.A., Semiatin, S.L., 2003. Handbook of Workability and Process Design. ASM international.
[40] An, X.H., Lin, Q.Y., Wu, S.D., Zhang, Z.F., 2010. Microstructural evolution and shear fracture of Cu–16at% Al alloy induced by equal channel angular pressing. Mater. Sci. Eng. A 527, 4510–4514.
[41] An, X.H., Lin, Q.Y., Wu, S.D., Zhang, Z.F., Figueiredo, R.B., Gao, N., Langdon, T.G., 2011. Significance of stacking fault energy on microstructural evolution in Cu and Cu–Al alloys processed by high-pressure torsion. Philos. Mag. 91, 3307–3326.
[42] Kunčická, L., Kocich, R., Hervoches, C., Macháčková, A., 2017. Study of structure and residual stresses in cold rotary swaged tungsten heavy alloy. Mater. Sci. Eng. A 704, 25–31.
[43] Vázquez-Fernández, N.I., Nyyssönen, T., Isakov, M., Hokka, M., Kuokkala, V.T., 2019. Uncoupling the effects of strain rate and adiabatic heating on strain induced martensitic phase transformations in a metastable austenitic steel. Acta Mater. 176, 134–144.
[44] Lee, S., Im, Y.-D., Matsumoto, R., Utsunomiya, H., 2021. Strength and electrical conductivity of Cu-Al alloy sheets by cryogenic high-speed rolling. Mater. Sci. Eng. A 799, 139815.
[45] Gray III, G.T., Follansbee, P.S., Frantz, C.E., 1989. Effect of residual strain on the substructure development and mechanical response of shock-loaded copper. Mater. Sci. Eng. A 111, 9–16.
[46] J.D. Embury, M.S. Szczerba, Z.S. Basinski, Twinning in advanced materials. Warrendale, PA: The Minerals. Metals and Materials Society, 1994.
[47] Huang, C.X., Wang, K., Wu, S.D., Zhang, Z.F., Li, G.Y., Li, S.X., 2006. Deformation twinning in polycrystalline copper at room temperature and low strain rate. Acta Mater. 54, 655–665.